ISSN: 2476- 2334

Research Article

International Journal of Nanotechnology & Nanomedicine

Easy Synthesis Method of MoS_2/TiO_2 Nanostructure with Great Performance of Catalytic Activity Under Visible Light

Sara Chahid*, Rodrigo Alcántara, and Desireé M de los Santos

Facultad de Ciencias, Universidad de Cádiz, Campus de Puerto Real, 11510, Puerto Real, (Cádiz), Spain

***Corresponding author**
Sara Chahid, Facultad de Ciencias, Universidad de Cádiz, Campus de Puerto Real, 11510, Puerto Real, (Cádiz), Spain, E-mail: sara10chahid@email.com

Submitted: 04 Jan 2019; **Accepted:** 10 Jan 2019; **Published:** 23 Apr 2019

Abstract

In this study, TiO_2 nanoparticles modified with MoS_2 were synthesized using the low temperature hydrolysis method. Samples of pure TiO_2 and samples of MoS_2/TiO_2 were prepared using different amounts of MoS_2 (1.0% and 10.0% by weight). The samples were annealed at 500°C and 700°C and characterised by ICP-AES, XRD, Raman, FT-IR, TG, XPS and DR-UV-Vis spectroscopy. The results suggest that the MoS_2 added during synthesis is a satisfactory source of Mo to produce doping of the TiO_2 structure. In addition, the transformation of anatase phase to rutile is delayed when the concentration of Mo incorporated into the structure increases. Finally, the effectiveness of the synthesized MoS_2/TiO_2 samplesused as photocatalyst for the photodegradation of methylene blue dye under visible light irradiation was investigated. TiO_2 doped with MoS_2 was shown to improve the degradation of methylene blue under visible light. There was found to be an optimal temperature and level of doping to achieve improved photocatalytic activity, in our case 10.0% MoS_2/TiO_2 at 700°C.

Keywords: Photoelectrochemisty, Photocatalyst, Structural Analysis, Spectroscopy

Introduction

Photocatalysis has become established as a promising technology for water treatment and is widely applied for purifying polluted water. In recent years, titanium dioxide (TiO_2) has been considered an excellent photocatalyst due to its good long-term stability against photo and chemical corrosion, low cost and lack of toxicity [1,2]. However, the band gap of TiO_2 is in the UV range of the electromagnetic spectrum, which is a limitation in photocatalytic applications as it only uses a small fraction of solar radiation. Society is demanding efficient methods for eliminating pollutants, one way being to extend the photo-response range of TiO_2 towards the visible region to improve its photocatalytic efficiency. Many strategies have been used to improve the photocatalytic properties of TiO_2, including forming hetero-structures (FeO_3-TiO_2, SnO_2-TiO_2, etc.), or doping with non-metals (N, F, etc.), or metals. The use of transition metals such as Cu, Cr, Ni, V, Fe, for doping TiO_2 has been widely researched [3-21]. Although less common, TiO_2 doped with Mo has been shown to have great potential as a photocatalyst [22-24]. In this study, TiO_2 was synthesized using the low-temperature hydrolysis method with MoS_2 as the source of Mo. An analysis was performed of the influence of the percentage of doping and the annealing temperature on the structural, electronic and optical properties of the nanoparticles synthesized. In addition, the appearance of the Burstein-Moss effect in the highly doped samples, characterized by a shift towards the blue end of the absorption spectrum, was also analysed [25]. Finally, a study was carried out into the influence of these properties on photocatalytic efficiency by means of the photodegradation of methylene blue under visible light.

Experimental

Chemicals

All the reagents were from commercial sources and used without further purification. Titanium (IV) n-butoxide (TNB, 97%) was from Sigma-Aldrich; nitric acid (HNO_3, 65%) was from Merck; and MoS_2 powder was from Sigma-Aldrich; and methylene blue (MB, purity 82%) was supplied by Panreac.

Synthesis

MoS_2/TiO_2 samples were synthesized using a low temperature hydrolysis reaction by means of a procedure reported previously by the authors [26]. (a) 100 mL of deionized H2O was cooled at 4°C in order to slow down the hydrolysis reaction, and in same time to control the crystallinity of the samples. (b) During the cooling process 4°C, a stoichiometric amount of MoS_2 was added to obtain theoretical proportions of x%MoS_2/TiO_2 (x% = 1.0%, 10.0% of MoS_2 added). (c) after that, 10 mL of n-butoxide source was slowly dripped into the mixture under magnetic stirring and the samples allowed to react for 30 min. (d) then, 4 mL of HNO_3 was added, and the mixture was stirred for 2 h; (e) after this, a rotavapor was used to evaporated the surplus solvent under vacuum at 60°C, and subsequently on a hotplate at 100°C until complete removal.

Finally, as-prepared MoS_2/TiO_2 samples were annealed in air for 1 h at 500°C and 700°C.

Also, pure TiO_2 was synthesized using the same procedure in order

to compare the results obtained.

Characterization

To characterize the pure TiO_2 and MoS_2/TiO_2 samples and to understand how MoS_2 affected their photocatalytic properties, different instrumental techniques were used to determine the proportion of MoS_2 and its location in the structure, their crystalline phases and band gap energy.

The composition of the MoS_2/TiO_2 samples was studied by inductively coupled plasma atomic emission spectroscopy (ICP-AES) using an Iris Intrepid spectrometer, supplied by Thermo Elemental©. Also, the identification of the crystalline phases and estimation of the crystallite size was performed by x-ray diffraction (XRD) using an instrument supplied by Bruker©, model D8Advanced. The XRD spectra were recorded with 2θ in the 20-70° range by step scanning, using steps of 0.02º, a fixed counting time of 0.1 s/ step, 40 kV and 30 mA. The characterization was completed using Raman spectroscopy. Raman spectra were registered in a backscattering geometry using a Jobin Yvon U1000 double monochromator equipped with a Hamamatsu R-943 photomultiplier, using a DPSS 532 nm laser supplied by CNI©, model MSL-III-532nm-50mW. Also, XPS experiments were performed using monochromatized Al Kα radiation (1486.6 eV), and a 20 eV pass energy to record the spectra. The binding energy scale was referred to the C1s signal at 284.8 eV, and given with an accuracy of 0.1 eV. The spectra were collected using a Kratos Axis UltraDLD spectrometer. Moreover, UV-Vis spectroscopy in diffuse reflectance mode (DR-UV-Vis) was used to study the optical properties of the samples and to determine the band gap energy. The equipment, assembled in our laboratory, was composed of a Xenon lamp, model ASB-XE-175, supplied by Spectral Products©, as the illumination source; a USB2000+ spectrometer supplied by Ocean Optics©; and an integrating sphere from Spectra Tech©. Finally, the photocatalytic activity of the MoS_2/TiO_2 samples synthesized was analysed. The evaluation of the photodegradation of methylene blue (MB) was performed using a halogen lamp as the visible irradiation source. The initial concentration of the aqueous solution of MB (purity 82%, Panreac) was 4·10-5 M, and the amount of photocatalyst was 0.3 gL-1. The reaction time was 6 hours, and the mixture of the photocatalyst and MB solution was kept in darkness for 3 hours before the VIS irradiation to reach the adsorption-desorption equilibrium. The photodecomposition of MB was studied using the concept of Degradation = (A0-At)/A0, where A0 is the initial absorbance at the start of the test and At is the absorbance at time t, both measured at 663.97 nm. The absorbance was measured using a spectrometer supplied by Ocean Optics©, model USB4000+, and a UV-VIS-NIR light source supplied by Ocean Optics©, model DH-2000-BAL [27].

Results and Discussion

ICP-AES

ICP-AES was used to determine the amount of Mo introduced into the MoS_2/TiO_2 heterostructure synthesized. The theoretical MoS_2/TiO_2 weight proportions added were 1.0%, and 10.0%. The percentages of Mo in the synthesized samples annealed at 500°C and 700°C are shown in Table 1. ICP analysis indicated that 45-64% of the Mo sources had been successfully introduced into the TiO_2 structure. However, the percentage of Mo incorporated with regard to that added was seen to decrease slightly as the percentage of MoS_2 added in the synthesis increased.

Table 1: Real weight percentage of Mo versus TiO_2 determined by ICP-AES

Initial %MoS_2 added	T / ºC	Mo (%w/w)	% Mo incorporated (%w/w)
0.0%	500 °C	≤0.10*	-
	700 °C	≤0.10*	-
1.0 %	500 °C	0.59 ± 0.02	59.0%
	700 °C	0.64 ± 0.04	64.0%
10.0%	500 °C	4.45 ± 0.01	44.5%
	700 °C	5.50 ± 0.10	55.0%

*Percentage lower than the detection limit of analytical method

XRD analysis

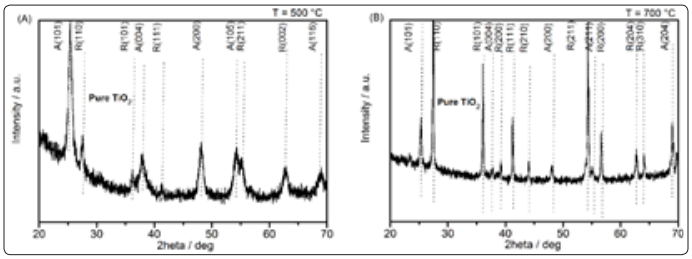

Figure 1: XRD patterns of pure TiO_2 annealed at (A) 500 °C and (B) at 700°C

It is well known that the crystallinity and crystalline phase of the titanium dioxide TiO_2 semiconductor strongly based on the annealing temperature [27]. This, could have a positive impact on photocatalytic activities. The XRD patterns of the TiO_2 powders annealed at different temperatures in air for 1 hour are displayed in Figure 1. As Figure 1 shown all obtained samples are crystalline. Further, the XRD pattern of pure TiO_2 calcined at 500°C exhibited the intense diffraction peak at 2θ = 25.5° which IS assigned to anatase phase, also a few peaks related to rutile phase was detected, this implied the coexistence of both anatase-rutile phases of TiO_2 in the sample annealed at 500°C [28,29]. However, this peak become more and more weaker as the annealing temperature increased, as Figure 1B displayed. Further, a peak with high intensity was appeared at 2θ=27.3°, which correspond to rutile phase [30]. Additionally, the characteristic diffraction peaks in this sample become more. This found results indicating that the crystallinity level was improved.

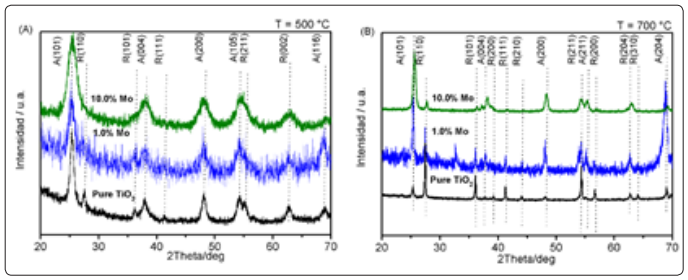

Figure 2: XRD patterns of pure TiO_2 and MoS_2/TiO_2 as-prepared samples annealed at (A) 500 °C and (B) at 700 °C.

The XRD study of the MoS_2/TiO_2 with different amount of MoS_2 (0.0, 1.0, and 10.0%) after thermal treatment was performed, which confirmed the transformation of the synthetized samples from amorphous phase to a crystalline phase, as Figure 2 depicted. The XRD diffraction peaks of pure TiO_2 calcined at 500°C contains a

mixture of anatase and rutile phase as discussed above. However, for MoS_2/TiO_2 samples, the diffraction peaks at 2θ= 25.4°, 27.2°, 36.5°, 38.7°, 48.3°, 55.1°, 55.2°, 64.2°,and 67.3°,which consistent with (101), (100), (101), (004), (200), (105), (211), (002)and (116) planes respectively, those signals are good matching to the anatase phase and reference (File No. JCPDS: 21-1272) [31]. Moreover, the widths of the main diffraction peak of anatase in MoS_2/TiO_2 become broadening, suggesting a clear decrease in particle size [32].

With the increase in temperature to 700°C, the peak assigned to rutile phase detected in pure TiO_2, was disappeared in MoS_2/TiO_2 samples, and all the diffraction peaks belong to anatase phase still present, which confirms that the MoS_2 added stabilize the anatase phase of TiO_2 even dough at high annealing temperatures. Interestingly, no evidence of any additional peaks assigned to MoS_2 phases such as, MoO_2, and TiS_2, were detected to be present in the XRD patterns of the synthesized samples. That could be a good indication of effective dispersion of MoS_2 due to their small crystallite particle size, finding results confirmed the structure of unique crystal phase of MoS_2/TiO_2 was successfully synthetized [33]. Further, the intrinsic structure of TiO_2 was kept after annealing process.

Further, from the XRD patterns, a semi-quantitative assessment was performed of several crystalline properties, such as the percentage of anatase (WA) and rutile (WR) phases, the average crystallite size (t) and the unit cell volume (V). The average crystallite size (t) was calculated from the full width at half-maximum (FWHM) according to the Scherrer equation: $t=(0.9\cdot\lambda)/\beta\cdot\cos\theta$, where λ is the wavelength of the X-Ray radiation (1.5406 Å) and β is the full width at half-maximum height of the most intense peak of the sample[34]. The relative contents of anatase (WA) and rutile (WR) phase given in mass fraction were estimated using the relative intensity of the rutile (110) peak using the following formula: $WR=1/(1+1.81\cdot IA/IR)$ and the relative contents of anatase were estimated as WA=100-WR; that is, only anatase and rutile phases were considered [34]. IA and IR are the relative intensities of the (101) peak of anatase and (110) peak of rutile, respectively. Furthermore, the volume of the unit cell was calculated from the values of the lattice constant a, b and c corresponding to the maximum intensity peak as $V = a^2\cdot c$ ($a = b \neq c$, for anatase and rutile phases). The values of a and c were estimated from the two peaks in the patterns with the highest intensity using the typical equation for tetragonal systems: $1/d^2= [(h^2+k^2)/ a^2] + (l^2/c^2)$, where d is the interplanar distance from Bragg's law, and h, k, l are the Miller indexes of the planes used [34,35]. The values obtained for these properties are shown in Table 2. The incorporation of MoS_2 delayed the anatase-to-rutile transformation, anatase being the predominant phase in the samples annealed at 500°C and 700°C, while rutile was the predominant phase only in the pure TiO_2 annealed at 700°C. Also, according to the semi-quantitative estimation of the amount of anatase and rutile phase, the percentage of rutile phase decreased when the amount of Mo increased.

Table 2: Semi-quantitative values of anatase and rutile mass fraction, average crystallite size, unit cell volume obtained from XRD patterns of the samples synthesized

T / °C	MoS_2 / %	WA / %	WR / %	t / nm	a, b / Å	c / Å	V / Å³
500 °C	0.0	62.39	37.61	10.91	3.81	8.90	129.32
	1.0	100.00	0.00	7.53	3.79	9.51	136.26
	10.0	100.00	0.00	3.50	3.78	9.13	130.54
700 °C	0.0	19.21	80.79	27.00	4.59	2.77	58.38
	1.0	55.90	44.10	21.04	3.78	9.60	137.20
	10.0	76.90	23.10	16.69	3.76	9.14	129.40

Table 2 shows the values of the average crystallite size (t) as a function of the annealing temperature; the higher the annealing temperature, the higher t, because of particle fusion of the nanocrystals. On the other hand, the evolution of t in relation to the percentage of MoS_2 added showed that t decreased as the percentage of MoS_2 increased. The introduction of Mo into the structure can create structural distortions that break the crystal continuity, thereby obtaining smaller average crystallite sizes, as reported for other dopants, such as Al, Cu or Tm. Thus, doping with Mo inhibits crystal growth and delays the transformation of anatase to rutile [11, 36-39].

Moreover, the peaks can be seen to shift and widen (Figure 1). As the ionic radius of Mo ions (0.62 Å) is very similar to that of Ti ions (0.68 Å), the Mo ions could substitute Ti ions in the TiO_2 lattice and the distortions observed may be a result of this [40,41]. However, in the 10.0% MoS_2/TiO_2 samples the loss of crystallinity was not as significant. Analysing the cell parameters of pure TiO_2 and MoS_2/TiO_2 shown in Table 2, it is possible to see that parameters a and c change slightly and the volume of the MoS_2/TiO_2 cells decreases as the percentage of MoS_2 increases, the cell volume of the 10.0% MoS_2/TiO_2 sample becoming similar to that of the pure TiO_2. This suggests that as the level of doping increases, the Mo may diffuse towards the surface of the crystal producing a structural reorganisation in which the Mo is distributed near to the surface, the interior being left with a lower Mo content [42]. Consequently, it has less tension, which would explain the greater crystalline quality observed in the 10% MoS_2/TiO_2 samples.

SEM analysis

Figure 3 presented SEM image of the synthetized MoS_2/TiO_2 nanoparticles. Homogenous clusters with pores were formed in the MoS_2/TiO_2 nanoparticles as SEM image displayed. The particle size of the MoS_2/TiO_2 porous structure is in nano-metric scale.

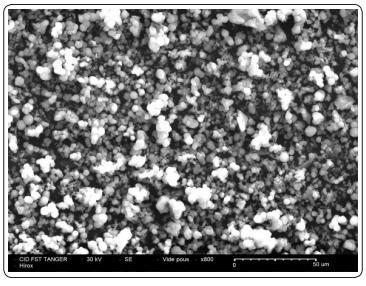

Figure 3: SEM image of the synthetized MoS_2/TiO_2 nanoparticles

The chemical composition of the synthetized samples was study using EDS analysis, the obtained EDS spectra is presented in Figure 4. As can be seen Figure 4, the MoS_2/TiO_2 nanoparticles mainly contained Mo, Ti, S, and O.

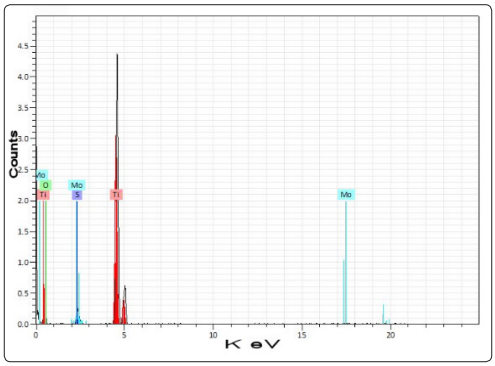

Figure 4: EDS analysis of the synthetized MoS_2/TiO_2 nanoparticles

Raman analysis

Figure 5 displayed the Raman spectra of the pure TiO_2 and MoS_2/TiO_2 synthesized samples annealed at 500°C (Figure 5A) and at 700°C (Figure 5B). TiO_2 is a semiconductor material type-n, which is full of vacancy defects [43]. Raman spectra of the synthesized samples displayed anatase and rutile phases of TiO_2. Specifically, anatase shows six Raman active modes: Eg (1), Eg (2), B1g (1), A1g+B1g (2), and Eg (3) at 144 cm^{-1}, 197 cm^{-1}, 399 cm^{-1}, 519 cm^{-1}, and at 639 cm^{-1} [44].

However, rutile phase presented four active Raman modes: B1g, Eg, A1g, and B2g at 143 cm^{-1}, 477 cm^{-1}, 612 cm^{-1} , 826 cm^{-1} [45]. Finding results indicate that Mo ions were well dispersed into TiO_2 lattice structure. Further, broadening and blueshift were observed in the main anatase peak Eg (1) in samples.

In addition, at 700°C plus the shift observed in Eg (1), peaks at 510 cm^{-1} and 630 cm^{-1} seem to displaced towards higher band, also this effect indeed increased with introduced Mo amount concentration augmented. Thus, confirm the successful substitution of Ti by Mo ions, which generates the tensions and distortions in the crystalline structure.

As a consequence, decrease in particle size and shift in the Raman bands [26,46-49]. The Raman spectra results are in good accordance with the XRD analysis discussed above.

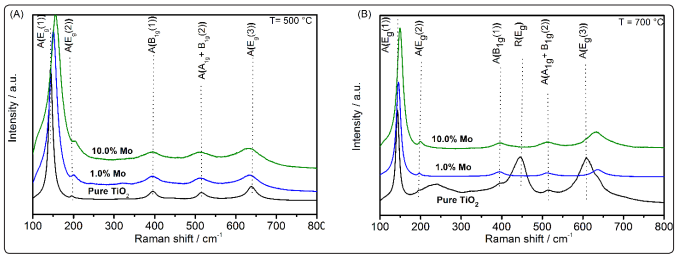

Figure 5: Raman spectra of the synthesized samples annealed at: (A) 500°C, (B) 700°C.

UV-Vis spectroscopy analysis

To investigate the optical response of the pure TiO_2 and MoS_2/TiO_2 synthesized samples, the diffuse reflectance spectra (DRS) of the nanoparticles powder were recorded.

Figure 6A and B presented the UV-Vis spectra in (DRS) for the pure TiO_2 and MoS_2/TiO_2 with different amount MoS_2 concentration (1.0%, and 10.0%) annealed at 500°C and at 700 °C, respectively. Figure 6 A and B presented the Tauc plot using Kubelka-Munk equation of different samples depicting Kubelka-Munk plots, where Figure 6C and D displayed the corresponding $([F(R).hv]^{1/2})$ against energy plot for the estimation of indirect band gap of the synthesized samples annealed at 500°C and at 700°C [50-52].

The effective indirect band gap of the synthesized samples was obtained by the extrapolation of the linear portion at $[F(R).hv]^{1/2} = 0$ [53,54]. The pure TiO_2 nanoparticles show a large fundamental absorption edge at around 775 nm which attributed to intrinsic indirect band gap of the TiO_2 [55]. The MoS_2/TiO_2 samples exhibited a broad blue shift absorption edge compared with pure TiO_2. The incorporation of MoS2 onto TiO_2 crystal lattice, lead to a significant increase of the visible light absorption due to the MoS_2 quantum confinement effect. With narrow band gap energy (1.23 eV), MoS_2 material consider as an excellent candidate for the solar light-driven applications [56]. Again, the bulk MoS_2 had a small band gap 1.23 eV, corresponding to the absorption edge at long wavelength (λ = 1040 nm) [57].

However, the MoS_2 in nano-scale, i. e., nanoparticles ranging from 8 nm to 10 nm, showed the adsorption in visible sunlight zone with wavelength approximately around 700 nm, while when the particle size decrease further, the absorption wavelength observed at 470 nm [58]. The particle size of the obtained MoS_2/TiO_2 nanoparticles under this study, varying from 27 nm to 3.5 nm. As a results, the absorption edge of the synthesized samples has been extended to visible region of the sunlight spectrum [59]. It was reported in literature that the strong quantum confinement effect observed in MoS_2 nanoparticles was responsible of the wide blue shifts observed in those samples [60-63]. Interestedly, also the quantum confinement effect is responsible for the shift observed in the redox potential and of the.

Table 3: Band gap energy values for the pure TiO_2 and MoS_2/TiO_2 samples synthesized

T / °C	Initial % MoS_2 added	E_g / eV
500	0.0	2.93
700		2.98
500	1.0	2.72
700		2.75
500	10.0	2.50
700		2.73

Table 3 shows the calculated band gap values of the pure TiO_2 and MoS_2/TiO_2 nanoparticles calcined at various temperatures (500°C and 700°C). The effective intrinsic band gap of TiO_2 was found decreased after the incorporation of MoS_2, that might be beneficial to reach a high performance of the visible light photodegradation of organic dye methylene blue. Due to the combination between TiO_2 and MoS_2 nanoparticles structures, the strong band bending at the interface improved and become more efficient entre TiO_2 and MoS_2 porous nanoparticles. So, the obtained MoS_2/TiO_2 nanostructures would be highly sensitive to the visible sunlight irradiation with the expectation of the enhancement of the visible light driven

photodegradation of methylene blue.

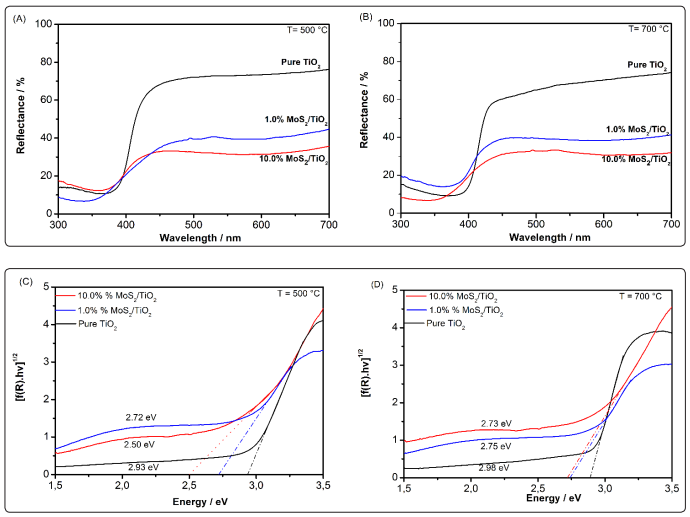

Figure 6: Absorption edge of the pure TiO_2 and MoS_2/TiO_2 synthesized samples annealed at: (A) 500°C, (B) 700°C. The corresponding Tauc plot of the synthesized samples annealed at (C) 500°C and (D) 700°C, considering the intrinsic band gap of TiO_2 as reference.

XPS analysis

The XPS spectra of pure TiO_2 and 5.5% MoS_2/TiO_2 were recorded. Figure 7a shows the Ti 2p peaks. Pure TiO_2 shows two peaks located at binding energies (BE) of 458.7 eV and 464.4 eV corresponding to Ti $2p_{3/2}$ and Ti $2p_{1/2}$ states of stoichiometric TiO_2, respectively, which is consistent with the values of Ti^{4+} in TiO_2 lattice reported in the literature.

The typical value reported for Ti(IV) is 458.66 eV, while for Ti(III), Ti(II) and Ti(0) they are 457.13 eV, 455.34 and 453.86 eV [64]. In turn, the distance between the BE of Ti $2p_{3/2}$ and Ti $2p_{1/2}$ was around 5.71 eV, which is consistent with previous results for Ti(IV) [65].

For the 5.5% MoS2/TiO_2 samples annealed at 500 °C and 700 °C, the binding energies of Ti $2p_{3/2}$ and Ti $2p_{1/2}$ were 459.18-459.93 eV and 464.93 eV, respectively, which are consistent with the presence of Ti^{4+} in the TiO_2.

The shift of the peaks towards a higher binding energy observed in the 5.5% MoS_2/TiO_2 samples with regard to pure TiO_2 may be caused by Mo, which may be an indication that Mo did indeed substitute Ti atoms in TiO_2 lattice [41,66].

Mo $3d_{3/2}$ and $3d_{5/2}$ peaks of the 5.5% MoS_2/TiO_2 sample annealed at 500°C and 700°C are shown in Figure 7(b). The Mo 3d signal shows the presence of a doublet peak structure at 235.67-236.05 eV and 232.92-232.93eV for the samples annealed at 500°C and 700°C, characteristic of Mo^{6+} ions [67,68].

The separation between the two peaks is around 2.8-3.1 eV, in agreement with the values reported in the literature [41,69]. The typical value for Mo $3d_{5/2}$ reported for Mo(VI) is 232.5 eV, while for Mo(IV) and Mo(V) they are 229.7 eV and 231.4 eV.47 No Mo^{4+} or Mo^{5+} peaks were observed, indicating that the main oxidation state of Mo in the samples was +6 [70].

The XPS spectra of O 1s for pure TiO_2 and 5.5% MoS_2/TiO_2 annealed at 500°C and 700°C (Figure 7(c)) show a signal composed of a main peak and another less intense contribution at a higher binding energy. For pure TiO_2, the O 1s signal can be decomposed into two peaks; the main peak located at a binding energy about 529.5 eV is assigned to O2− in TiO_2 lattice, and the small left shoulder peak at about 530.8 eV to adsorbed species, such as hydroxyl groups, or water [71].

Further, for the 5.5% MoS_2/TiO_2 samples, a wider, asymmetric peak shifted towards a higher binding energy is observed. The peak located at a binding energy of 530.3-530.4 eV is assigned to O2− in the lattice linked to Mo (OMo−O) [72,73]. Furthermore, an increase is observed in the signal of the peak assigned to adsorbed species, suggesting that the doping produced charge deficiency in the structure. Since a titanium atom needs two oxygen atoms, and a molybdenum atom needs three oxygen atoms, the structure is oxygen deficient.

This can be compensated for by oxygen atoms absorbed onto the surface of the doped sample[41], atoms that are beneficial to photocatalytic activity [74].

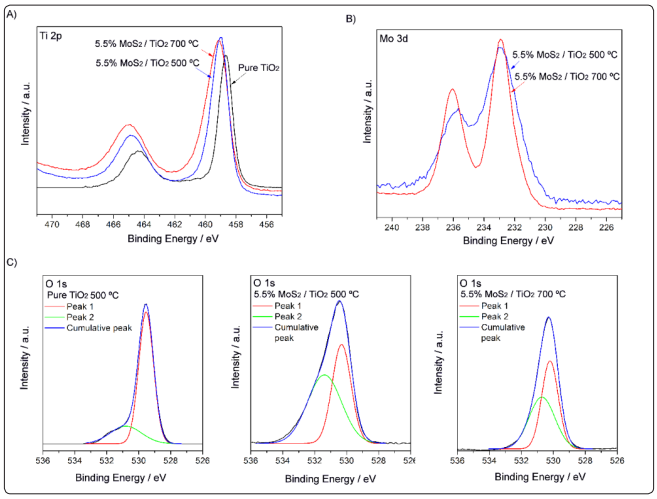

Figure 7: XPS spectra for samples synthesized of Ti 2p (a), Mo3d (b) and O 1s (c)

The photocatalytic activity mechanism of MoS_2/TiO_2 nanoparticles

The photocatalytic efficiency of the MoS_2/TiO_2 samples annealed at 500°C and 700°C were studied by means of the photodegradation of methylene blue under visible light.

A blank experiment without a catalyst was performed and no significant degradation of the MB was found.

In addition, to determine the time taken to reach the adsorption-desorption equilibrium a preliminary test was performed involving keeping the mixture of the photocatalyst and MB solution in the dark for 8 hours. The samples reached the adsorption-desorption equilibrium in 3 hours.

Therefore, to analyse the photodegradation of the MB, the samples were kept in the dark for 3 hours and after this time the irradiation with visible light began. The irradiation time was 6 hours and the test lasted 9 hours in total.

For comparison purposes, the measurements of the photodegradation of the methylene blue were performed using the pure, synthesized TiO_2 photocatalyst and commercial TiO_2 (Degussa P25) under the same conditions.

The results of total degradation after 6 hours of visible light irradiation are shown in Table 4.

Table 4: Percentage of photodegradation of methylene blue using the photocatalysts studied under visible light after 6 hours of irradiation

Photocatalyst	Un-annealed	T = 500 °C	T = 700 °C
P25 TiO_2	40.1%	-	-
Pure TiO_2	-	34.6%	24.2%
1.0%MoS_2/ TiO_2	-	64.7%	73.0%
10.0%MoS_2/ TiO_2	-	85.1%	87.4%

Figure 8 shows the evolution with the irradiation time of the percentage of degradation of the MB photocatalyst for the samples under study.

A degradation of up to 40.1% can be observed for the P25 sample, somewhat higher than for the pure TiO_2 samples synthesized and annealed at 500ºC and 700ºC. In turn, the percentage degradation of MB increased when using the samples that incorporate Mo (see Table 4). For the samples annealed at 500ºC, a percentage degradation of approximately up to 85% is observed for the sample incorporating 10.0% of MoS_2.

However, the photocatalytic activity of the samples annealed at 700°C is greater than that of the samples annealed at 500°C, except for the pure TiO_2 samples. In this case the difference can be attributed to the greater presence of rutile phase, which is less active.

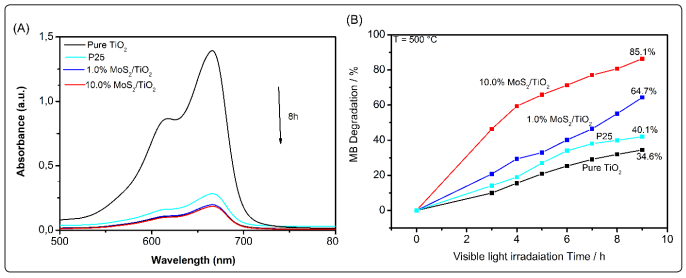

Figure 8: Visible spectra of synthesized samples (A), and (B) photodegradation of methylene blue under visible light irradiation using the synthesized samples as photocatalyst

The results from DRX and Raman spectroscopy show that the samples annealed at 700°C had greater crystallinity than those annealed at 500°C. Good crystallinity is very important in photocatalytic activity because it results in better movement of the charge carriers [75]. Further, the recombination between TiO_2 with MoS_2 was favorable thermodynamically, and due to the presence of Mo ions, successful separation of photoexcited electron-hole pairs prolonged the lifetime of photoexcited pairs. Thus effectively suppressed the recombination of electron-hole pairs, resulting an enhance the photocatalytic activity of TiO_2.

Additionally, although the predominant phase was anatase, in the samples annealed at 700°C there was also a certain amount of rutile phase (Table 2). The heterojunction in the phases in the doped samples contributed to the charge separation, reducing the recombination of electron-hole pairs and thus improving photocatalytic activity [76-79].

In turn, particle size is known to be an important parameter influencing photocatalytic efficiency. The electron-hole recombination rate may depend on the particle size. Table 2 shows that the particle size (t) decreased as the percentage of Mo increased. It is well known that in the nanometer-size range, the physical and chemical properties of semiconductors are modified (compared with bulk). Small variations in particle diameters lead to great modifications in the surface/bulk ratio, thus influencing the recombination rates of volume and surface electrons and holes [80]. A smaller particle size also produces a greater specific surface. After doping, the Mo^{6+} ions replace Ti^{4+} ions in the TiO_2 lattice, creating an oxygen deficiency that may be compensated by oxygen atoms absorbed onto the surface of the doped sample [41]. In addition, the Mo^{6+} ions can act as electron traps to promote charge separation, thus reducing the recombination rate of the photogenerated carriers [69]. These photogenerated electrons trapped by Mo^{6+} may be transfered to the oxygen molecules adsorbed onto the surface, which would get the necessary electrons to form H_2O_2, HO_2-and O_2^- species that also enhance photocatalytic activity [41,81]. However, among the photocatalysts annealed at a 700°C, the photocatalytic activity of 1.0% MoS_2/TiO_2 (85%) was slightly lower than the 10.0% MoS_2/TiO_2 sample (87%) [82].

Further, the kinetic reaction of the synthesized samples was investigated, and the photodegration of methylene blue followed first-order kinetics, the K_{app} which is the apparent kinetic reaction rate constant was obtained by the use of the formula (1):

$$ln\ C_0/\ C_t = K_{app}\ t, \qquad (1)$$

where C_0 and C_t are the concentration of methylene blue at time = 0 and at t.

Table 5 displayed the obtained values of K_{app} of each catalyst used for methylene blue degradation measurements. When the experimental data fitted with formula 1, the apparent constant reaction rate (K_{app}) for the methylene blue degradation were calculated to be 0.0004, 0.0453, 0.1139, 0.1577, and 4.7853h-1 for methylene blue in absence of catalyst, pure TiO_2, P25, 1.0% MoS_2/ TiO_2, and 10.0% MoS_2/ TiO_2, respectively.

Additionally, the photocatalytic performance of MoS_2/TiO_2 nanoparticles for methylene blue degradation under sun light irradiation was 5 times faster than that of pure TiO_2.

Table 5: The obtained apparent constant reaction rate constant K_{app} values

Catalysts	K_{app} (h^{-1})
Without catalyst	0.0004
Pure TiO_2	0.0453
P25	0.1139
1.0%MoS_2/ TiO_2	0.1577
10.0%MoS_2/ TiO_2	4.7853

Therefore, the result observed for the synthetized sample suggests that the MoS_2/TiO_2 nanoparticles samples can be an excellent candidate as photocatalyst for the degradation of MB under visible light irradiation when it compared with pure TiO_2, as Figure 9 displayed. According to reports, the photocatalytic mechanism within MoS_2/TiO_2 nanoparticles could be explained by following reasoning; under visible light irradiation, the electron could be transited from the conduction band (CB) of MoS_2 nanoparticles to CB of TiO_2 [59,61,83]. In aqueous solution, the photoexcited electron will scavenged by the oxygen coming from the water, which lead to generation of hydroxyl radicals and decontaminate the organic pollutants [83]. Due to presence of the elements N and S in the methylene blue ($C_{16}H_{18}CIN_3S$) colorant, so the complete degradation of this colorant can be expressed as follows:

$$O_2 + C_{16}H_{18}CIN_3S \rightarrow CO_2 + H_2O + SO_4^{2-} + NH^{4+}$$

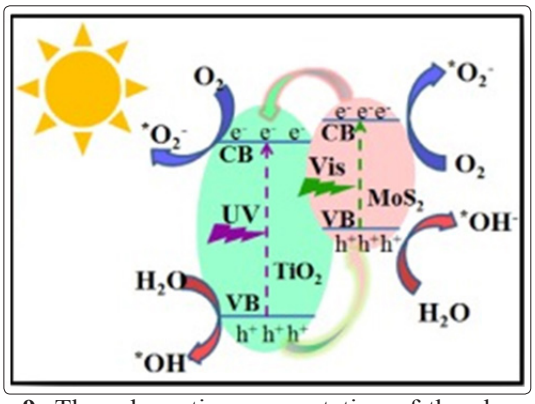

Figure 9: The schematic representation of the charge transfer mechanism in MoS_2/TiO_2 samples with improved photocatalytic activity compared with pure TiO_2 nanoparticles.

Conclusions

In summary, the synthesized MoS_2/TiO_2 nanoparticles with improved visible sun light driven photocatalytic activity were successfully obtained by the use of low temperature hydrolysis and their photocatalytic activity for the degradation of methylene blue were reported. Uniform morphology and decrease in particle size were obtained in synthesized MoS_2/TiO_2 nanoparticles samples. The highest photocatalytic activity was showed by the sample with 10.0% MoS_2/TiO_2 nanoparticle annealed at 700°C, since it has the appropriate amount of MoS_2 concentration for suppressing recombination of the photogenerated electron-hole and prolonged the electron life-time. Indeed, the 10.0% MoS_2/TiO_2 nanoparticles show highest value of the apparent photocatalytic reaction rate constant about 4.85 times highest than that of pure TiO_2 sample. Thus, founding results indicated that this work study could be extended to improve the performance and quality for solar light-driven applications.

References

1. Lee AC, Lin RH, Yang CY, Lin MH, Wang WY (2008) Mater Chem Phys 109: 275-280.
2. Weng ZY, Guo H, Liu XM, Wu SL, Yeung KWK, et al. (2013) Rsc Adv 3: 24758-24775.
3. Ghorai T K, Chakraborty M, Pramanik P (2011) J Alloy Compd 509: 8158-8164.
4. Cao H, Huang S L, Yu Y L, Yan Y B, Lv YK (2017) J Colloid Interf Sci 486: 176-183.
5. Guo Q, Zhang ZH, Ma XP, Jing K, Shen ML, et al. (2017) Separation and Purification Technology 175: 305-313.
6. Ryu SW, Kim E J, Ko SK, Hahn SH (2004) Mater Lett 58: 582-587.
7. Shakir S, Khan Z S, Ali A, Akbar N, Musthaq W (2015) J Alloy Compd 652: 331-340.
8. Zhou W, WL, Wang J, Qu Y, Yang Y, et al. (2014) J Am Chem Soc 136: 9280-9283.
9. Krishnakumar V, Boobas S, Jayaprakash J, Rajaboopathi M, Han B, et al. (2016) Journal of Materials Science-Materials in Electronics 27: 7438-7447.
10. Zhou L, Wei LG, Yang YL, Xia X, Wang P, et al. (2016) Chem Phys 475: 1-8.
11. Navas J, Sanchez-Coronilla A, Aguilar T, De los Santos DM, Hernandez NC (2014) Nanoscale 6: 12740-12757.
12. Nishiyama N, Kozasa K, Yamazaki S (2016) Appl Catal a-Gen 527: 109-115.
13. Wojtaszek K, Tyrala K, Czapla-Masztafiak J, Sa J, Szlachetko J (2016) Chem Phys Lett 664: 73-76.
14. Zhu JL, Xia XF, Zhu SS, Liu X, Li HX (2016) Chem J Chinese U 37: 1833-1839.
15. Fu YH, Sun L, Yang H, Xu L, Zhang FM, et al. (2016) Appl Catal B-Environ 187: 212-217.
16. Haider AJ, Najim AA, Muhi MAH (2016) Optics Communications 370: 263-266.
17. Singla P, Pandey OP, Singh K (2016) International Journal of Environmental Science and Technology 13: 849-856.
18. Zhang DR, Jin XZ, Li JH (2016) Mater Chem Phys 176: 68-74.
19. Beauger C, Testut L, Berthon-Fabry S, Georgi F, Guetaz L (2016) Microporous and Mesoporous Materials 232: 109-118.
20. Birben NC, Uyguner-Demirel CS, Sen Kavurmaci S, Gurkan YY, Turkten N, et al. (2017) Catal Today 281: 78-84.
21. Wang QY, Jin RC, Zhang M, Gao SM (2017) J Alloy Compd 690: 139-144.
22. Di Paola A, Garcia-Lopez E, Marci G, Marti C, Palmisano L, et al. (2004) Appl Catal B-Environ 48: 223-233.
23. Devi LG, BNM (2008) Characterization of Mo doped TiO_2 and its enhanced photo catalytic activity under visible light Catal Lett 125: 320-330.
24. Li CX, Zhang D, Jiang ZH, Yao ZP, Jia FZ (2011) New J Chem 35: 423-429.
25. Munir S, Shah SM, Hussain H, Ali khan R (2016) Materials & Design 92: 64-72.
26. Alcántara R, Navas J, Fernández-Lorenzo C, Martín J, Guillén E, et al. (2011) Phys Status Solidi C Curr Top Solid State Phys 8: 1970-1973.
27. Cheng L, Kang Y, Tong F (2012) Effect of preparation conditions on characteristics of hollow TiO_2 fibers fabricated by chemical deposition and template method Appl Surf Sci 263: 223-229.
28. Wan Q, Duan L, He K, Li J (2011) Removal of gaseous elemental mercury over a CeO_2– WO_3/TiO_2 nanocomposite in simulated coal-fired flue gas, Chemical Engineering Journal 170: 512-517.
29. Wu Z, Tang N, Xiao L, Liu Y, Wang H (2010) MnOx/TiO_2 composite nanoxides synthesized by deposition–precipitation method as a superior catalyst for NO oxidation, Journal of Colloid and Interface Science 352: 143-148.
30. Shi J, Chen S, Wang S, Ye Z, Wu P,et al. (2010) Favorable recycling photocatalyst TiO_2/ CFA: effects of calcination temperature on the structural property and photocatalytic activity, Journal of Molecular Catalysis A: Chemical 330: 41-48.

31. Liu H, Dong XN, Liu TT, Su X, Zhu ZF (2014) Mater Lett 115: 219-221.
32. Zainal ND, Nur H, Lee SL (2015) Synthesis and characterization of nitrogen-doped titania nanomaterials of homogeneous particle size 11: 13-15.
33. Rezaei E, Soltan J (2012) Low temperature oxidation of toluene by ozone over MnOx/γ- alumina and MnOx/MCM-41 catalysts, Chemical Engineering Journal 198-199: 482-490.
34. Landmann M, Rauls E, Schmidt WG (2012) J Phys-Condens Mat 24.
35. Maurya A, Chauhan P, Mishra SK, Srivastava RK (2011) J Alloy Compd 509: 8433-8440.
36. de los Santos DM, Navas J, Sánchez-Coronilla A, Alcántara R, Fernández-Lorenzo C.
37. de los Santos DM, Navas J, Sánchez-Coronilla A, Alcántara R, Fernández-Lorenzo C (2015) Mater Res Bull 70: 704-711.
38. Xu L, Garrett MP, Hu B (2012) J Phys Chem C 116: 13020-13025.
39. Aguilar T, Navas J, Alcantara R, Fernandez-Lorenzo C, Gallardo JJ, et al. (2013) Chem Phys Lett 571: 49-53.
40. PD by Robert C Weast, Handbook of Chemistry & Physics 59th Edition 1978-1979, CRC Press Inc 1979.
41. Wang S, LNB, Sun HM, Jiang Q, Lian JS (2013) Powder Technol 244: 9-15.
42. Richardson PL, Perdigoto MLN, Wang W, Lopes RJG (2013) Appl Catal B-Environ 132: 408-415.
43. Paul KK, Ghosh R, Giri PK (2016) Mechanism of strong visible light photocatalysis by Ag2O-nanoparticle-decorated monoclinic TiO2 (B) porous nanorods, Nanotechnology 27: 315703.
44. Patel SKS, Gajbhiye NS, Date SK (2011) J Alloy Compd 509: S427-S430.
45. Mathews NR, Morales ER, Cortes-Jacome MA, Antonio JAT (2009) Sol Energy 83: 1499-1508.
46. Zaki MI, AK, Muftah AI, Jagadale TC, Ikram M, Ogale SB (2013) Appl Catal a-Gen 452: 214-221.
47. Kang MS (2005) Mater Lett 59: 3122-3127.
48. Zhan CC, Chen F, Yang JT, Dai DX, Cao XH (2014) J Hazard Mater 267: 88-97.
49. de los Santos DM, Aguilar T, Sanchez-Coronilla A, Navas J, Hernandez NC, et al. (2014) Chemphyschem 15: 2267-2280.
50. Diamandescu L, Vasiliu F, Tarabasanu-Mihaila D, Feder M, Vlaicu AM, et al. (2008) Mater Chem Phys 112: 146-153.
51. Murphy AB (2007) Sol Energ Mater Sol Cells 91: 1326-1337.
52. Serpone N, Lawless D, Khairutdinov R (1995) Size effects on the photophysical properties of colloidal anatase TiO_2 particles e size quantization or direct transitions in this indirect semiconductor J Phys Chem-Us 99: 16646e-16654.
53. Sasca V, Popa A (2013) J Appl Phys 114.
54. Serpone N, Lawless D, Khairutdinov R (1995) J Phys Chem 99: 16646-16654.
55. Zaki MI, Mekhemer GAH, Fouad NE, Jagadale TC, Ogale SB (2010) Mater Res Bull 45: 1470-1475.
56. Ho W, Yu JC, Lin J, Yu J, Li P (2004) Preparation and photocatalytic behavior of MoS2 and WS2 nanocluster sensitized TiO_2, Langmuir 20: 5865-5869.
57. Kam KK, Parkinson BA (1982) J Phys Chem 86: 463-467.
58. Thurston TR, Wilcoxon JP (1999) J Phys Chem B 103: 11.
59. Pourabbas B, Jamshidi B (2008) Chem Eng J 138: 55-62.
60. Wilcoxon JP, Newcomer PP, Samara GA (1997) J Appl Phys 81: 7934-7944.
61. Wilcoxon JP (2000) J Phys Chem B 104: 7334-7343.
62. Huang JM, Laitinen RA, Kelley DF (2000) Phys Rev B 62: 10995.
63. Thurston TR, Wilcoxon JP (1999) J Phys Chem B 103:11-17.
64. Biesinger MC, LWML, Gerson AR, Smart RSC (2010) Appl Surf Sci 257: 887-898.
65. Savio AKPD, Fletcher J, Hernandez FCR (2013) Ceram Int:39: 2753-2765.
66. Huang JG, XTG, Wang B, Li LY, Zhao MX et al. (2015) Journal of Spectroscopy 1-8.
67. Zhu SS, YMD, Xia XF, Liu X, Li HX (2016) Rsc Adv 6: 23809-23815.
68. Nguyen NH, Wu HY, Bai HL (2015) Chem Eng J 269: 60-66.
69. Khan H, Berk D (2014) Journal of Photochemistry and Photobiology A: Chemistry 294: 96-109.
70. Erdogan N, Park J, Ozturk A (2016) Ceram Int 42: 16766-16774.
71. Kang M, Lee MH (2005) Appl Catal A Gen 284: 215-222.
72. Li N, Li Y, Zhou Y, Li W, Ji S, et al (2017) Sol Energ Mat Sol C 160: 116-125.
73. Lu M, Shao C, Wang K, Lu N, Zhang X, et al (2014) ACS Applied Materials and Interfaces 6: 9004-9012.
74. Huang JG, Guo XT, Wang B, Li LY, Zhao MX, et al. (2015) Journal of Spectroscopy 1-8.
75. De los Santos DM, Navas J, Aguilar T, Sanchez-Coronilla A, Fernandez-Lorenzo C,et al. (2015) Beilstein J Nanotechnology 6: 605-616.
76. Huang LH, Chan QZ, Zhang B, Wu XJ, Gao P, et al. (2011) Chinese J Catal 32: 1822-1830.
77. Chimupala Y, Junploy P, Hardcastle T, Westwood A, Scott A, et al. (2016) Journal of Materials Chemistry A 4: 5685-5699.
78. Scanlon DO, Dunnill CW, Buckeridge J, Shevlin SA, Logsdail AJ, et al. (2013) Nature Materials 12: 798-801.
79. Ohtani B, Prieto-Mahaney OO, Li D, Abe R (2010) J Photoch Photobio A 216: 179-182.
80. Zhou M, JYaBC (2006) J Hazard Mater 137: 1838-1847.
81. Simonsen ME, Li ZS, Sogaard EG (2009) Appl Surf Sci 255: 8054-8062.
82. Luo S-Y, Yan B-X, Shen J (2012) Thin Solid Films 522: 361-365.
83. Ho WK, Yu JC, Lin J, Yu JG, Li PS (2004) : Langmuir 20: 5865.